Journal of *Marine Science and Engineering*

MDPI

Article

Analysis of Power Performance and Wake Interference in a Three-Turbine Tandem Array of Offshore Wind Turbines

Chengwei He [1], Hao Hu [1], Jiaqi Jia [1], Zhuang Shen [2], Zhihao Zhang [3], Jiahuang Tu [1,4,*] and Zhaolong Han [5]

[1] College of Civil Engineering, Xiangtan University, Xiangtan 411105, China; 202421653029@smail.xtu.edu.cn (C.H.); 202421652991@smail.xtu.edu.cn (H.H.); 202405651324@smail.xtu.edu.cn (J.J.)
[2] School of Mechanical Engineering and Mechanics, Xiangtan University, Xiangtan 411105, China; shenzhuang1995@yeah.net
[3] School of Hydraulic and Ocean Engineering, Changsha University of Science & Technology, Changsha 410114, China; zzh_well@csust.edu.cn
[4] Hunan Provincial Key Laboratory of Dynamic Loading Characteristics and Engineering Toughness of Materials, Xiangtan 411105, China
[5] School of Ocean and Civil Engineering, Shanghai Jiao Tong University, Shanghai 200240, China; han.arkey@sjtu.edu.cn
* Correspondence: tujiahuang1982@163.com

Abstract

This study investigates multiple-wake interactions and downstream power losses in a heterogeneous tandem array comprising DTU 10-MW and NREL 5-MW offshore wind turbines. TurbSim is used to generate turbulent inflow fields, and a three-turbine tandem array is simulated in FAST. Farm using the Dynamic Wake Meandering model. Seven turbine configurations and 57 simulation scenarios are considered to systematically examine the effects of streamwise spacing, inflow turbulence intensity, turbine-type combination, and turbine-type arrangement on power output and wake evolution. The results show that increasing the streamwise spacing generally improves the power output and wake power retention ratios of the intermediate and downstream turbines. Compared with uniform inflow, turbulent inflow with a prescribed turbulence intensity of 15% generally enhances momentum exchange across the wake shear layers, accelerates wake recovery, and reduces downstream power losses, although its effect on total array power depends on the turbine configuration. Turbine-type arrangement affects downstream performance by changing the spatial extent of the wake generated by the intermediate turbine and its vertical overlap with the rotor-swept area of the downstream turbine. At a streamwise spacing of $5D_{ref}$ and a turbulence intensity of 15%, placing the NREL 5-MW turbine at the intermediate position and the DTU 10-MW turbine downstream results in a downstream wake power retention ratio of 53.2%. Reversing their positions reduces this ratio to 31.9%. Nevertheless, the corresponding total array powers differ by only 0.3 MW because the power outputs are redistributed between the intermediate and downstream turbines. These findings demonstrate that streamwise spacing, inflow conditions, and turbine-type arrangement should be considered jointly when evaluating the wake recovery and power performance of heterogeneous offshore wind-turbine arrays.

Keywords: horizontal-axis wind turbine; heterogeneous wind turbines; tandem array; turbine layout; wake recovery

Check for updates

Received: 8 October 2026
Revised: 31 October 2026
Accepted: 2 November 2026
Published: 4 November 2026

Copyright: © 2026 by the authors. Licensee MDPI, Basel, Switzerland. This article is an open access article distributed under the terms and conditions of the Creative Commons Attribution (CC BY) license.

1. Introduction

Offshore wind capacity and turbine ratings have increased rapidly as countries pursue decarbonization targets [1,2]. As wind farms become larger and more densely clustered, wake interactions increasingly constrain energy production. The wake velocity deficit and elevated turbulence generated by an upstream turbine reduce the effective inflow velocity and produce nonuniform loading on downstream turbines [3].

Previous studies have shown that streamwise spacing affects wake development and recovery, as well as the extent of multiple-wake superposition, thereby altering the effective inflow velocity and power output of downstream turbines. Stevens et al. [4] conducted theoretical analyses and numerical simulations and demonstrated that larger streamwise spacing weakens wake effects on downstream turbines and increases their power output. However, these benefits gradually diminish once the spacing exceeds a certain threshold. Based on large-eddy simulations of the atmospheric boundary layer, Niayifar et al. [5] reported a clear relationship between wake recovery and streamwise spacing, showing that larger spacing promotes turbulent mixing and accelerates wake recovery.

Bastankhah et al. [6] developed a Gaussian analytical wake model based on the conservation of mass and momentum. The model predicts that wake width increases approximately linearly over a certain downstream range, while the centerline velocity deficit progressively decreases. This provides a theoretical basis for evaluating the effects of streamwise spacing on downstream inflow conditions. Baas et al. [7] employed atmospheric large-eddy simulations to investigate multi-gigawatt offshore wind farms and showed that compact layouts intensify wake overlap and increase overall wind-farm power losses, whereas larger streamwise spacing mitigates these adverse effects. From the perspective of deep-array effects, Bay et al. [8] similarly showed that small streamwise spacing exposes downstream turbines to persistent multiple-wake effects, thereby limiting wake recovery and reducing power output, while larger streamwise spacing improves downstream performance. Kirby et al. [9] further noted that streamwise spacing affects not only local wake superposition but also farm-scale momentum transport and, consequently, the spatial distribution of power losses.

Inflow conditions, particularly turbulence intensity, are critical to wake recovery and downstream power recovery. Recent studies have examined the mechanisms by which inflow turbulence affects wind-turbine wake evolution. Wang et al. [10] investigated the effects of different wind-farm layouts under turbulent inflow and showed that appropriate spatial arrangement of turbines can mitigate wake shielding and improve downstream power recovery. Vahidi et al. [11] proposed a physics-based wake-expansion model based on atmospheric-boundary-layer turbulence and showed that higher inflow turbulence intensity enhances momentum exchange in the wake shear layer, thereby accelerating wake diffusion and recovery. Hodgson et al. [12] further examined the effect of inflow turbulence time scales and found that different time scales can alter near-wake breakdown, wake recovery, and the rotor-averaged inflow velocity of downstream turbines even at comparable overall turbulence intensities. Gambuzza et al. [13] analyzed wake development under free-stream turbulence and reported that high turbulence intensity combined with small turbulence time scales promotes faster wake evolution, whereas larger turbulence scales may delay recovery. In addition, Hu et al. [14] numerically investigated the aerodynamic performance and wake evolution of a coaxial co-rotating dual-rotor wind turbine, focusing on inter-rotor aerodynamic coupling, blade-motion parameters, and turbulent mixing. Their work provides a useful reference for understanding wake mechanisms in complex wind-turbine systems.

Variable hub-height designs bring benefits for wind farms. They reduce vertical wake overlap. They optimize incoming-flow status for downstream turbines. Uniform hub-height

layouts serve as a reference case. Multi-hub-height layouts create vertical misalignment for rotor-swept areas. They lower risks. The risk means downstream rotors are fully wrapped by upstream low-speed wake cores. Sun et al. [15,16] treated wind-farm planar layout and hub height as coupled optimization variables and showed that hub-height optimization changes wake coverage and downstream inflow distributions, thereby improving wind-farm power output. Their joint optimization of turbine number, hub height, and offshore array layout also demonstrated a clear coupling between hub height and planar position, indicating that planar optimization alone may not fully reduce wake losses. Unlike these studies, which focused mainly on engineering optimization and power enhancement, Ciavarra et al. [17] applied a gradient-based optimization method to wind farms with multiple hub heights and showed that multi-height configurations can expand the layout-design space and provide additional degrees of freedom for reducing wake interference.

Heterogeneous wind farms have also been investigated through multi-type layout optimization, coupled turbine-design and layout optimization, tandem-wake experiments, and hybrid offshore wake optimization [18–21]. However, fewer studies have used a common numerical case matrix to examine how streamwise spacing, prescribed inflow turbulence intensity, upstream turbine type, rotor-size and hub-height differences, and turbine-type arrangement jointly affect both turbine-level wakes and total power in a three-turbine tandem array. This gap is especially relevant offshore, where low ambient turbulence can prolong wakes and mixed-capacity deployment introduces differences in rotor diameter, hub height, aerodynamics, and control.

To address this gap, the present study considers an offshore three-turbine tandem array composed of two representative turbine types with different capacities, namely the DTU 10-MW and NREL 5-MW wind turbines. The effects of streamwise spacing, turbine-type combination and arrangement, and inflow conditions on aerodynamic performance and wake evolution are systematically investigated. Section 2 describes the numerical methods and validation, including momentum theory and the Betz limit, the Dynamic Wake Meandering model, turbulent-wind-field validation, mesh-independence assessment, and aerodynamic-performance validation. Section 3 presents the tandem-array model and the simulation cases for different spacings, turbine configurations, and inflow conditions. Section 4 investigates the effects of streamwise spacing, inflow conditions, and turbine-type arrangements on the power performance and wake characteristics of the tandem wind turbine array. Furthermore, the overall power performance of the entire array is evaluated by considering the combined power outputs of all three turbines, followed by a discussion of the scope and limitations of the present study. Section 5 summarizes the main findings and their implications for heterogeneous offshore wind-farm layout design.

2. Numerical Methods and Validation

2.1. Momentum Theory and the Betz Limit

Classical axial momentum theory represents a turbine as an ideal, uniformly loaded actuator disk in steady, incompressible, inviscid flow [22,23]. It relates induction, thrust and power under the assumptions of one-dimensional flow and equal far-upstream and far-wake static pressures. The following established relations provide background notation; they are not a new numerical method.

The axial velocity at the rotor plane is:

$$Ud = U_\infty(1 - \alpha) \tag{1}$$

The far-wake velocity is:

$$Uw = U_\infty(1 - 2\alpha) \tag{2}$$

The ideal power extracted by the wind turbine is:

$$P = TUd = 2\rho AdU_{\infty}^{3}\alpha\,(1-\alpha)^{2} \tag{3}$$

The dimensionless power coefficient C_p is:

$$Cp = \frac{P}{\frac{1}{2}\rho AdU_{\infty}^{3}} = 4\alpha\,(1-\alpha)^{2} \tag{4}$$

where α is the axial induction factor; ρ is the air density (kg m^{-3}); A_{∞}, A_d, and A_w are the streamtube cross-sectional areas in the far-upstream region, at the rotor plane, and in the far wake, respectively (m^2); and U_{∞}, U_d, and U_w are the corresponding axial velocities (m s^{-1}).

When the axial induction factor $\alpha = 1/3$, the power coefficient reaches its maximum value, with $C_{p,max}$ corresponding to the Betz limit.

2.2. Dynamic Wake Meandering (DWM) Model

The Dynamic Wake Meandering (DWM) model represents wake deflection, meandering, deficit evolution and wake superposition [24]. For a non-yawed turbine in uniform inflow, the mean wake is aligned with the wind direction. Large turbulent structures displace the wake laterally and vertically, while smaller structures contribute to mixing and deficit recovery. Under the approximately axisymmetric thin-shear-layer assumptions, the radial deficit gradient dominates the axial gradient, and the pressure-gradient term is neglected [25], giving the axial momentum equation:

$$rV_x\frac{\partial V_x}{\partial x} + rV_r\frac{\partial V_x}{\partial r} = vt\frac{\partial V_x}{\partial r} + rvt\frac{\partial^2 V_x}{\partial r^2} + r\frac{\partial vt}{\partial r}\frac{\partial V_x}{\partial r} \tag{5}$$

$$V_r + r\frac{\partial V_r}{\partial r} + r\frac{\partial V_x}{\partial x} = 0 \tag{6}$$

where V_x and V_r are the axial and radial mean velocity components (m s^{-1}), x and r are the axial and radial coordinates (m), and ν_t denotes the kinematic eddy viscosity (m^2 s^{-1}). Equations (5) and (6) express axial momentum transport and axisymmetric continuity, respectively.

Under the assumption of axial symmetry, wake transport is solved transiently on a polar wake plane using radial finite differences. A low-pass temporal filter separates the turbulent eddies in the wind field into large-scale structures larger than approximately twice the rotor diameter and small-scale structures smaller than this scale. Large-scale structures govern the trajectory of the wake center and therefore its meandering, whereas small-scale structures primarily influence wake-deficit evolution. Here, f_c is the cutoff frequency of the low-pass filter used in the wake-advection, deflection, and meandering calculations, and f_c must be greater than zero. The characteristic time scale and the corresponding cutoff frequency are defined as follows [24]:

$$\tau_1 = \frac{1.1}{1 - 1.3\min\left(a_{avg}, 0.5\right)}\frac{R}{U_{\infty}} \tag{7}$$

$$f_c = \frac{2.4}{\tau_1} \tag{8}$$

where τ_1 is the characteristic time scale, a_{avg} is the rotor-disk-averaged axial induction factor, and R is the wind-turbine rotor radius (m).

For heterogeneous wind farms, wake scales and recovery rates differ because turbines of different capacities can have different rotor diameters, hub heights, thrust coefficients,

and operating characteristics. FAST.Farm solves for the wake evolution separately for each turbine and evaluates multi-turbine interactions through local wake superposition, providing a unified framework for analyzing wake coupling among heterogeneous turbines.

The axisymmetric approximation for wake-deficit evolution applies locally to the wake of each individual turbine. Each wake is associated with the source turbine's own rotor position and hub height and is evaluated at the actual three-dimensional locations of downstream rotors. The approximation therefore does not require all turbines in the array to share a common global rotor axis.

In the following wake visualization results, the normalized streamwise velocity deficit is used to characterize wake recovery. It is defined as $\frac{\Delta U}{U_\infty} = \frac{\overline{U}-U_\infty}{U_\infty}$, where $\overline{U}$ denotes the time-averaged local streamwise velocity, and U_∞ denotes the axial velocity of the undisturbed incoming flow, consistent with its definition in Section 2.1. The streamwise coordinate is normalized by the reference rotor diameter, expressed as x/D_{ref}.

2.3. Numerical Validation

2.3.1. Turbulent Wind Field Validation

TurbSim is a numerical code used to generate stochastic full-field turbulent wind-speed time histories and is widely employed to model atmospheric-boundary-layer inflow for wind-turbine aeroelastic simulations. On a prescribed two-dimensional vertical grid, it generates three-dimensional velocity time series consisting of streamwise (u), cross-stream (v), and vertical (w) components [26]. These spatially and temporally correlated wind fields provide inflow boundary conditions for unsteady aerodynamic simulations at both turbine and wind-farm scales.

TurbSim was used to generate a turbulent wind field 235 m high and 2000 m wide, with a prescribed turbulence intensity of 15% and mean wind speed of 11.4 m/s. Figure 1 shows a representative spatiotemporal distribution. Figure 2 compares the streamwise-velocity spectrum at z = 119 m with the prescribed Kaimal spectrum. The TurbSim spectrum agrees well with the Kaimal spectrum over the principal frequency range, and the overall energy-distribution trends are consistent. The generated field therefore reproduces the main spectral characteristics of atmospheric-boundary-layer turbulence and is suitable as the inflow condition for the subsequent aerodynamic and wake analyses.

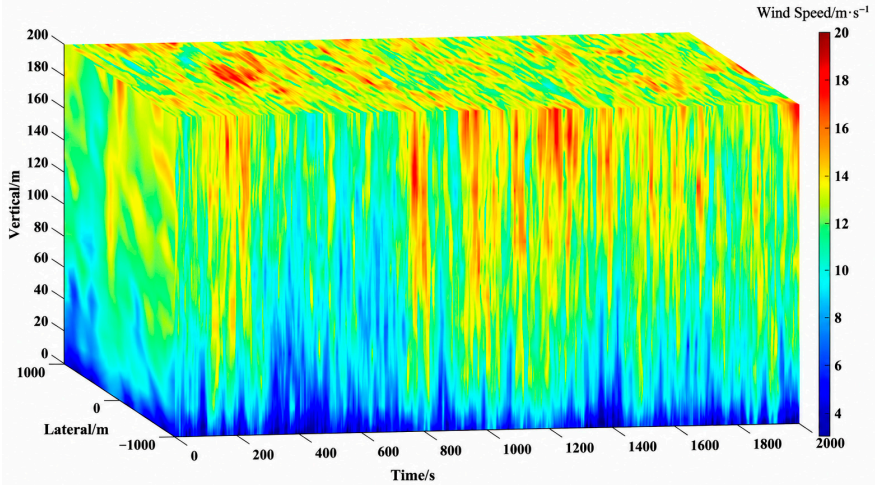


Figure 1. Spatiotemporal distribution of the turbulent wind field.

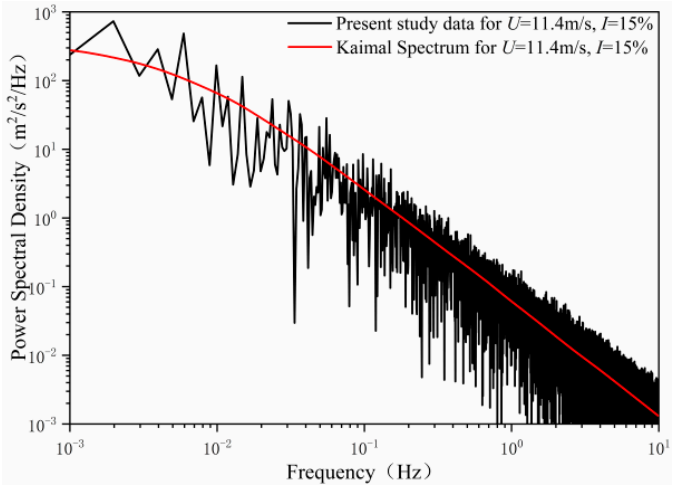


Figure 2. Comparison between the simulated wind-speed spectrum and the Kaimal spectrum at $U = 11.4$ m/s and $I = 15\%$.

2.3.2. Mesh-Independence Assessment

To reduce computational cost while maintaining adequate accuracy, FAST.Farm uses a multiscale computational-domain discretization in which the wind-farm flow field is represented by low-resolution and high-resolution domains [27]. The low-resolution domain covers the entire wind farm and resolves large-scale unsteady processes such as wake advection, deflection, diffusion, and multi-wake interaction. A finer high-resolution domain is defined around each turbine to resolve local inflow variation, near-rotor flow, and wake structures relevant to aerodynamic loads and power output. Coupling the low-resolution full-field domain with the high-resolution local domains substantially reduces the computational cost of wind-farm simulations while retaining the resolution required near individual turbines. In this study, the time step was set to 0.0125 s [10,28].

The existing spatial-sensitivity comparison uses a single NREL 5-MW turbine under uniform inflow at 11.4 m/s. To verify the grid independence of the numerical simulation results, simulations were performed for both the NREL 5-MW and DTU 10-MW wind turbines using different mesh sizes. The power outputs obtained from each mesh configuration were compared with the corresponding reference values reported in the literature [29,30]. As shown in Table 1, for the NREL 5-MW wind turbine, the output powers obtained using Meshes 1, 2, and 3 were 5.28 MW, 5.23 MW, and 5.22 MW, respectively, corresponding to power ratios of 99.81%, 98.87%, and 98.68%. For the DTU 10-MW wind turbine, the corresponding output powers were 9.94 MW, 9.92 MW, and 9.91 MW, with power ratios of 99.4%, 99.2%, and 99.1%, respectively. It can be observed that, for both wind turbines, the results obtained using Mesh 1 are closest to the reference values and exhibit the highest power ratios, indicating that this mesh configuration provides relatively high numerical accuracy. Therefore, considering the mesh comparison results for both wind turbines, Mesh 1 was selected for all subsequent numerical simulations.

Table 1. Comparison of wind-turbine power output for different mesh sizes.

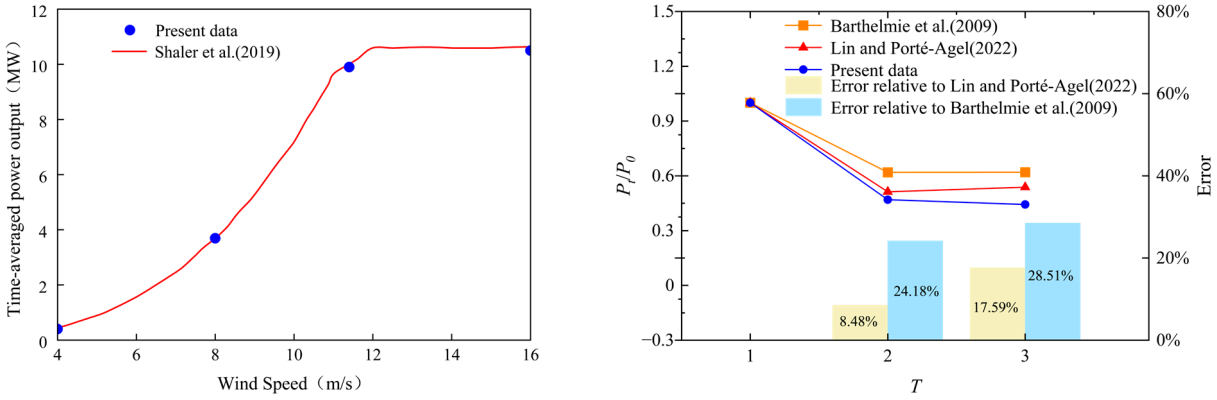
	Mesh	Low-Resolution Mesh Size (m)	High-Resolution Mesh Size (m)	Output Power (MW)	Power Ratio (%)
NREL 5-MW	Mesh 1	5	5	5.28	99.81
	Mesh 2	10	10	5.23	98.87
	Mesh 3	20	10	5.22	98.68
	Ref. [29]			5.29	100%

Table 1. *Cont.*

	Mesh	Low-Resolution Mesh Size (m)	High-Resolution Mesh Size (m)	Output Power (MW)	Power Ratio (%)
DTU 10-MW	Mesh 1	5	5	9.94	99.4
	Mesh 2	10	10	9.92	99.2
	Mesh 3	20	10	9.91	99.1
	Ref. [30]			10.0	100%

2.3.3. Validation of Single- and Multi-Turbine Aerodynamic Performance

Figure 3a compares the simulated power output of the DTU 10-MW turbine with the corresponding design values under different operating conditions. Below the rated wind speed and around the rated operating region, the simulated results agree well with the design curve, indicating that the numerical model adequately reproduces the power-response characteristics of the DTU 10-MW turbine under typical operating conditions.



(**a**) DTU 10-MW single-turbine case (**b**) NREL 5-MW multi-turbine case

Figure 3. Comparison between the present results and data reported in the literature [26,31,32].

Considering that the present study further addresses wake interactions and power prediction among multiple wind turbines within a wind farm, field measurements from the Horns Rev wind farm [31] and large-eddy simulation (LES) results [32] were introduced as reference benchmarks to evaluate the capability of the adopted model to reproduce power attenuation characteristics under multi-turbine array conditions. The comparison of power output among different turbines is shown in Figure 3b. Overall, the present numerical results are slightly lower than the LES results reported in Ref. [32], while the LES results are, in turn, lower than the field measurements reported in Ref. [31]. Nevertheless, all three datasets exhibit a generally consistent downstream power attenuation trend across the wind farm. Since the reference studies involve different turbine configurations and operating conditions, Figure 3b mainly provides a cross-study comparison of normalized power attenuation rather than a strict like-for-like quantitative validation.

As shown in Figure 3b, the maximum deviation occurs at turbine T3, where the present numerical predictions differ from the LES results and field measurements by 17.59% and 28.51%, respectively. For T2, the deviations from the LES results and field measurements are 8.48% and 24.18%, respectively, giving mean deviations of 13.04% and 26.35% across T2 and T3. Since T1 serves as the normalization reference, its zero deviation does not constitute an independent accuracy assessment.

Turbine T3 shows relatively large prediction error. Multiple-wake overlap brings strong flow non-uniformity and unsteadiness. These factors cause part of the error. Other factors

also exert influences. They include simulation software setups. They include boundary condition settings. They include wind-farm operational parameter gaps between this work and reference papers. All these items lead to power-prediction bias. For the field measurements, the results are additionally influenced by various environmental and operational factors, including ambient temperature, humidity, atmospheric stability, terrain roughness, and the actual operating status of the turbines, which are generally difficult to reproduce fully in numerical simulations. These factors may partly contribute to the differences between the numerical predictions and field measurements.

The wake velocity-deficit distributions presented in Section 4 provide complementary information for interpreting the simulated power variations, rather than independent quantitative validation of the wake flow field. Despite these quantitative discrepancies, the model captures the overall downstream power attenuation characteristics, supporting comparative analyses of wake evolution and power distribution under consistent simulation conditions.

3. Simulation Setup

3.1. Wind-Farm Layout and Computational Domain

Numerical simulations of a tandem wind-farm configuration were conducted using two horizontal-axis reference turbines with different rated capacities: the NREL 5-MW and DTU 10-MW turbines. To balance computational efficiency and local flow-field resolution, a two-level domain discretization was used. The outer low-resolution domain covers the entire wind farm and represents the overall flow and wake development, whereas a high-resolution domain surrounding each turbine improves resolution near the rotor and in the near wake. For all cases, the outer domain was 4000 m × 2000 m × 230 m. An independent high-resolution region of 200 m × 200 m × 225 m was defined around each turbine and nested within the outer domain. The principal turbine parameters are listed in Table 2, the tandem layout is shown in Figure 4, and the hub elevations of the four turbine configurations are illustrated in Figure 5.

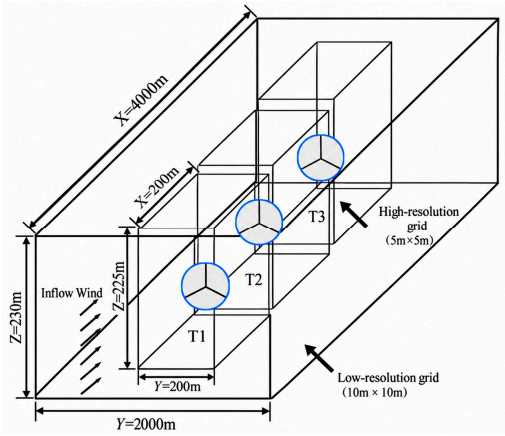


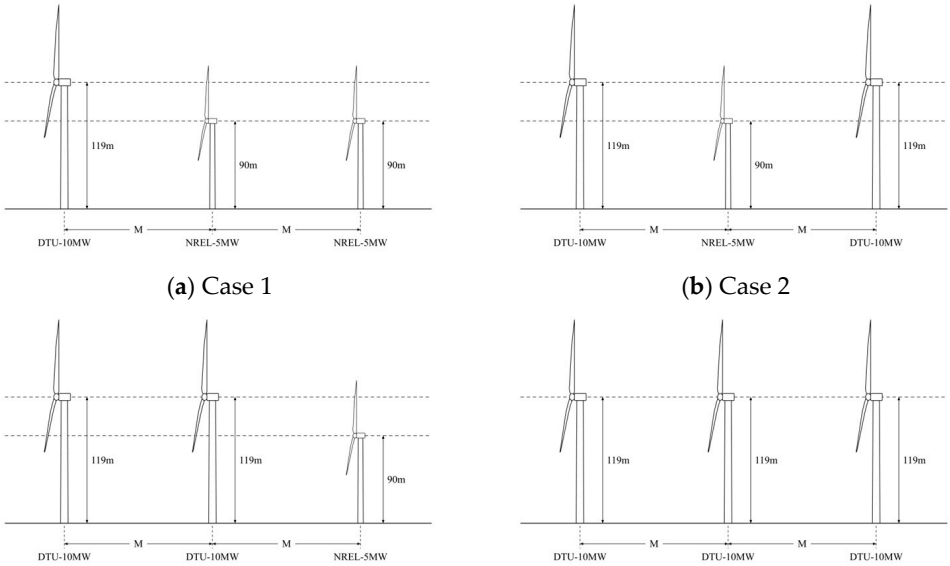
Figure 4. Three-dimensional schematic of the computational domain and tandem layout. Turbines are aligned only in plan view; turbine-specific hub heights are given in Table 2 and Figure 5.

Table 2. Main parameters of the NREL 5-MW and DTU 10-MW wind turbines.

Parameter	NREL 5-MW [29]	DTU 10-MW [30]
Cut-in wind speed (m/s)	3	4
Cut-out wind speed (m/s)	25	25
Rated wind speed (m/s)	11.4	11.4

Table 2. *Cont.*

Parameter	NREL 5-MW [29]	DTU 10-MW [30]
Rated power (MW)	5	10
Number of blades	3	3
Actual rotor diameter D_r (m)	126	178.3
Hub diameter (m)	3	5.6
Hub height (m)	90	119
Rotor mass (t)	110	228
Nacelle mass (t)	240	446
Tower mass (t)	347	628



(**a**) Case 1 (**b**) Case 2

(**c**) Case 3 (**d**) Case 4

Figure 5. Four turbine configurations with hub heights of 119 m for the DTU 10-MW turbine and 90 m for the NREL 5-MW turbine. Mixed-type configurations retain the 29 m vertical rotor-axis offset.

3.2. Simulation Cases and Operating Conditions

To further investigate the effects of different rated-power turbine-type arrangements on the overall power generation performance of the turbine array, three additional comparison cases were established under identical inflow wind speeds and streamwise spacing ratios. These cases were Case 5 (NREL 5-MW–DTU 10-MW–NREL 5-MW), Case 6 (NREL 5-MW–NREL 5-MW–DTU 10-MW), and Case 7 (NREL 5-MW–DTU 10-MW–DTU 10-MW). These configurations were designed to investigate the effects of different turbine capacity combinations and arrangement sequences on the array power output when an NREL 5-MW turbine was placed in the first row.

Cases 5–7 were included to permit direct comparisons with Cases 1–3 at the same installed capacities and streamwise spacings. Their total array power performance is evaluated together with that of Cases 1–4 in Section 4.4.

Cases 1–4 were simulated at $3D_{ref}$, $4D_{ref}$, $5D_{ref}$, and $8D_{ref}$ under uniform inflow and prescribed turbulence intensities of 8% and 15%, giving 48 case–spacing–inflow combinations. Cases 5–7 add nine uniform-inflow combinations at $3D_{ref}$–$5D_{ref}$, for a total of 57 combinations. Figure 5 illustrates Cases 1–4, and Table 3 lists all seven configurations and their operating conditions.

Table 3. Simulation cases and operating conditions.

Case	Upstream Turbine	Intermediate Turbine	Downstream Turbine	Streamwise Spacing, M	Inflow Condition
Case 1	DTU 10-MW	NREL 5-MW	NREL 5-MW	$3D_{ref}$, $4D_{ref}$, $5D_{ref}$, $8D_{ref}$	Uniform, $I = 8\%$, or $I = 15\%$
Case 2	DTU 10-MW	NREL 5-MW	DTU 10-MW		
Case 3	DTU 10-MW	DTU 10-MW	NREL 5-MW		
Case 4	DTU 10-MW	DTU 10-MW	DTU 10-MW		
Case 5	NREL 5-MW	DTU 10-MW	NREL 5-MW	$3D_{ref}$, $4D_{ref}$, $5D_{ref}$	Uniform
Case 6	NREL 5-MW	NREL 5-MW	DTU 10-MW		
Case 7	NREL 5-MW	DTU 10-MW	DTU 10-MW		

Regarding the wind-farm layout, although the IEC standards do not prescribe mandatory streamwise-spacing requirements, representative streamwise spacings are generally selected within typical engineering ranges for wind-farm design, wake assessment, and power-prediction studies. Accordingly, in the present study, the turbines were arranged sequentially along the incoming-flow direction, and the center-to-center spacing between adjacent turbines in the x direction was denoted by (M). Four streamwise spacings, $M = 3D_{ref}$, $4D_{ref}$, $5D_{ref}$, and $8D_{ref}$, were considered to systematically investigate the effects of turbine spacing on wake superposition and downstream power recovery. In this study, the rotor diameter of each turbine is denoted as D_r. The NREL 5-MW and DTU 10-MW turbines have rotor diameters of $D_{r,NREL} = 126$ m and $D_{r,DTU} = 178.3$ m, respectively. Because different turbine types are considered in the heterogeneous tandem array, a unified reference length is required for spacing normalization. Therefore, the rotor diameter of the NREL 5-MW turbine is selected as the reference diameter, defined as $D_{ref} = 126$ m.

Two inflow conditions were considered: ideal uniform inflow and turbulent inflow. The incoming wind was aligned with the positive x direction and was normal to the rotor planes. The selection of turbulence intensity is important for wind turbine wake simulations because turbulence characteristics are influenced by wind speed, measurement height, atmospheric stability, and surface roughness. Türk and Emeis [33] investigated the relationship between turbulence intensity and wind speed using four years of measurements from the FINO1 observation platform. Emeis [34] further reported that, at a measurement height of 90 m, the mean turbulence intensity reached a minimum of approximately 4.5% at a wind speed of 12 m/s, while the corresponding 90th-percentile values were approximately 7–8.5% within the wind-speed range of 10–12 m/s. Furthermore, Sørum et al. [35] conducted a statistical analysis of 15 years of measurements at a height of 100 m, reporting mean values of the fitted design turbulence-intensity distributions of approximately 9.20% and 8.82% for wind-speed ranges of 8–10 m/s and 14–16 m/s, respectively.

Based on these measurement results, two turbulent inflow conditions with turbulence intensities of 8% and 15% were selected in the present study [36]. The 8% turbulence intensity was adopted as an intermediate turbulence condition to investigate the effects of moderate turbulent disturbances on wake development and array power performance. The 15% turbulence intensity was retained as a relatively high turbulence sensitivity condition to examine the changes in wake evolution and array power performance under stronger turbulent mixing. Meanwhile, uniform inflow (0%) was retained as an idealized reference condition to facilitate comparisons of wake characteristics and power output under different turbulence intensities. It should be emphasized that the prescribed turbulence intensities are intended for comparative numerical analyses rather than being calibrated to the long-term statistical characteristics of a specific site. The principal TurbSim and FAST.Farm settings required for reproducibility are reported in Appendix A, and the notation used throughout the manuscript is summarized in Appendix B.

All simulation cases were run for a total duration of 2000 s. During the initial stage of each simulation, the turbine operating states and flow field had not yet reached statistically stationary conditions. To eliminate the influence of the initial transient response on the statistical results, the first 1000 s of simulation data were discarded, and only the final 1000 s were used for post-processing and statistical analysis, thereby ensuring the reliability and stability of the reported results [37].

4. Results and Discussion

4.1. Effects of Streamwise Spacing on Turbine Power Output

Figure 6 illustrates the effects of streamwise spacing on the time-averaged power output of the three-turbine tandem array under different turbine configurations and inflow conditions. Overall, increasing the streamwise spacing has a negligible effect on the power output of T1 but progressively improves the power generation of T2 and T3. Specifically, the power output of T1 remains approximately 9.9 MW, 9.3 MW, and 9.4 MW under uniform inflow, 8% turbulence intensity, and 15% turbulence intensity, respectively. This is because T1 is located upstream of the entire array and is therefore not affected by the wakes generated by the downstream turbines. In contrast, T2 and T3 exhibit substantial power recovery as the spacing increases from $3D_{ref}$ to $8D_{ref}$. For example, under uniform inflow, the power outputs of T2 and T3 in Case 1 increase from 1.4 and 1.0 MW to 2.3 and 2.5 MW, respectively. Similar increases are observed in the other three configurations, demonstrating that increasing streamwise spacing consistently improves the power output of downstream turbines.

To facilitate comparisons between turbines with different rated capacities, the normalized power output is defined as:

$$P^* = \frac{P_i}{P_{r,i}} \times 100\% \tag{9}$$

where P_i is the time-averaged power output of turbine i over the final 1000 s, and $P_{\square,i}$ is its rated power, corresponding to 5 MW for the NREL turbine and 10 MW for the DTU turbine. This parameter represents the fraction of rated power achieved by each turbine. However, rated-power normalization alone cannot directly quantify the power loss induced by wake interference because the two turbine types have different aerodynamic characteristics and rated capacities. Therefore, a wake power retention ratio is introduced to provide a more consistent evaluation of wake-induced power losses:

$$\eta_{i,wake} = \frac{P_{i,wake}}{P_{i,0}} \times 100\% \tag{10}$$

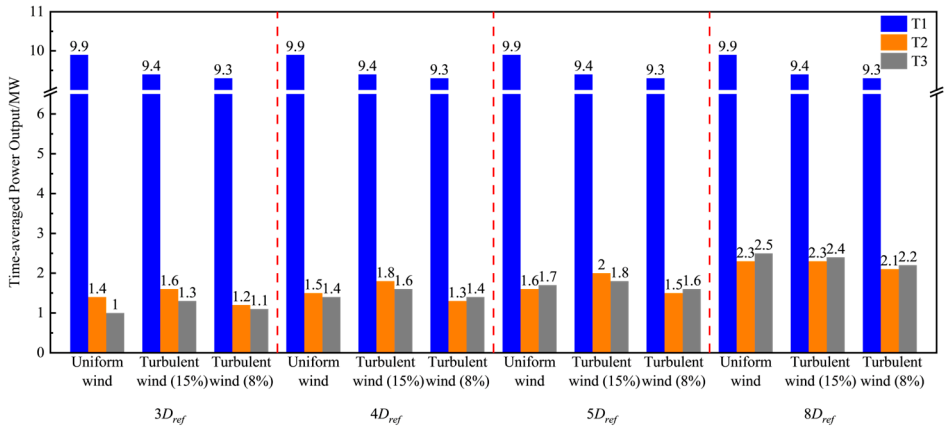
where $P_{i,wake}$ denotes the time-averaged power output of turbine i under wake-affected conditions, and $P_{i,0}$ represents the corresponding reference power output of the same turbine operating independently without upstream wake interference under identical inflow conditions. The reference power outputs of the NREL 5-MW turbine under uniform inflow, 8% turbulence intensity, and 15% turbulence intensity are 4.9, 4.6, and 4.7 MW, respectively. The corresponding values for the DTU 10-MW turbine are 9.9, 9.3, and 9.4 MW. Based on this definition, the wake-induced power loss ratio can be expressed as:

$$L_{i,wake} = 100\% - \eta_{i,wake} \tag{11}$$

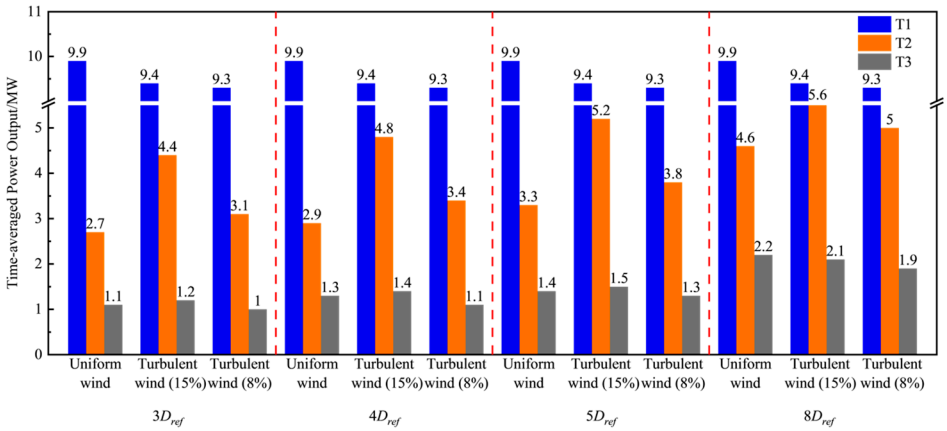
A higher wake power retention ratio indicates a smaller relative power loss caused by wake interference.

Figures 7a and 7b show the wake power retention ratios of T2 and T3 in Cases 1 and 2, respectively. Under uniform inflow, the retention ratios of T2 and T3 in Case 1 increase from 28.6% and 20.4% at $3D_{ref}$ to 46.9% and 51.0% at $8D_{ref}$, respectively. A similar trend is

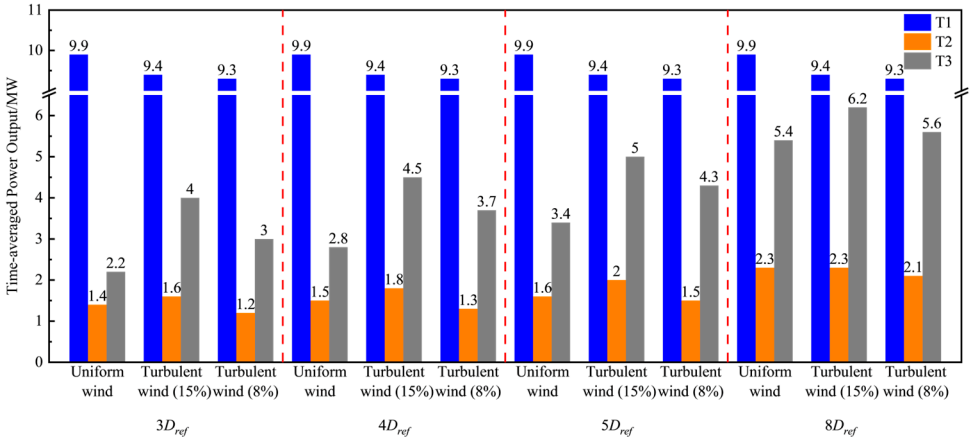
observed in Case 2, where the corresponding values increase from 28.6% and 22.2% to 46.9% and 54.5%. These results indicate that increasing streamwise spacing effectively reduces the relative power losses of downstream turbines. In particular, T3 exhibits a more pronounced improvement than T2 in both configurations, which can be attributed to its exposure to the cumulative effects of upstream wakes. As the spacing increases, the interaction between successive wakes becomes less severe, allowing the downstream turbine to recover a greater proportion of its corresponding isolated-turbine power output.



(**a**) Case 1

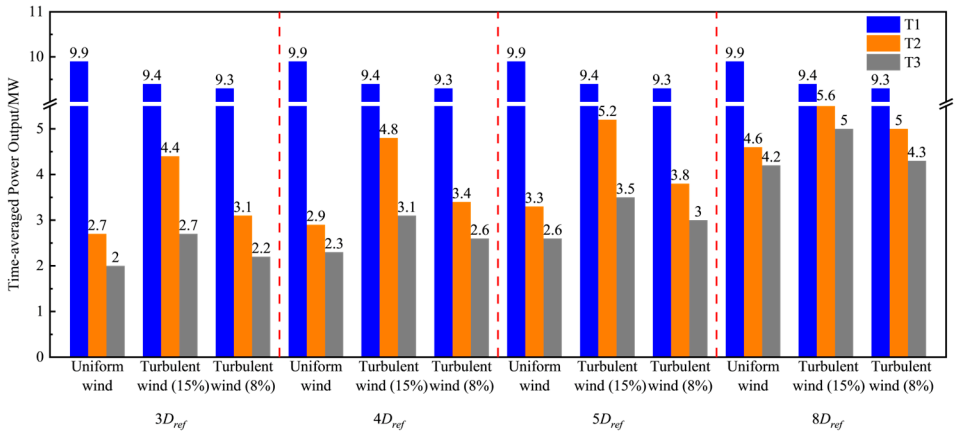


(**b**) Case 2



(**c**) Case 3

Figure 6. *Cont.*



(**d**) Case 4

Figure 6. Time-averaged power output of the three-turbine tandem array under different streamwise spacings and inflow conditions.

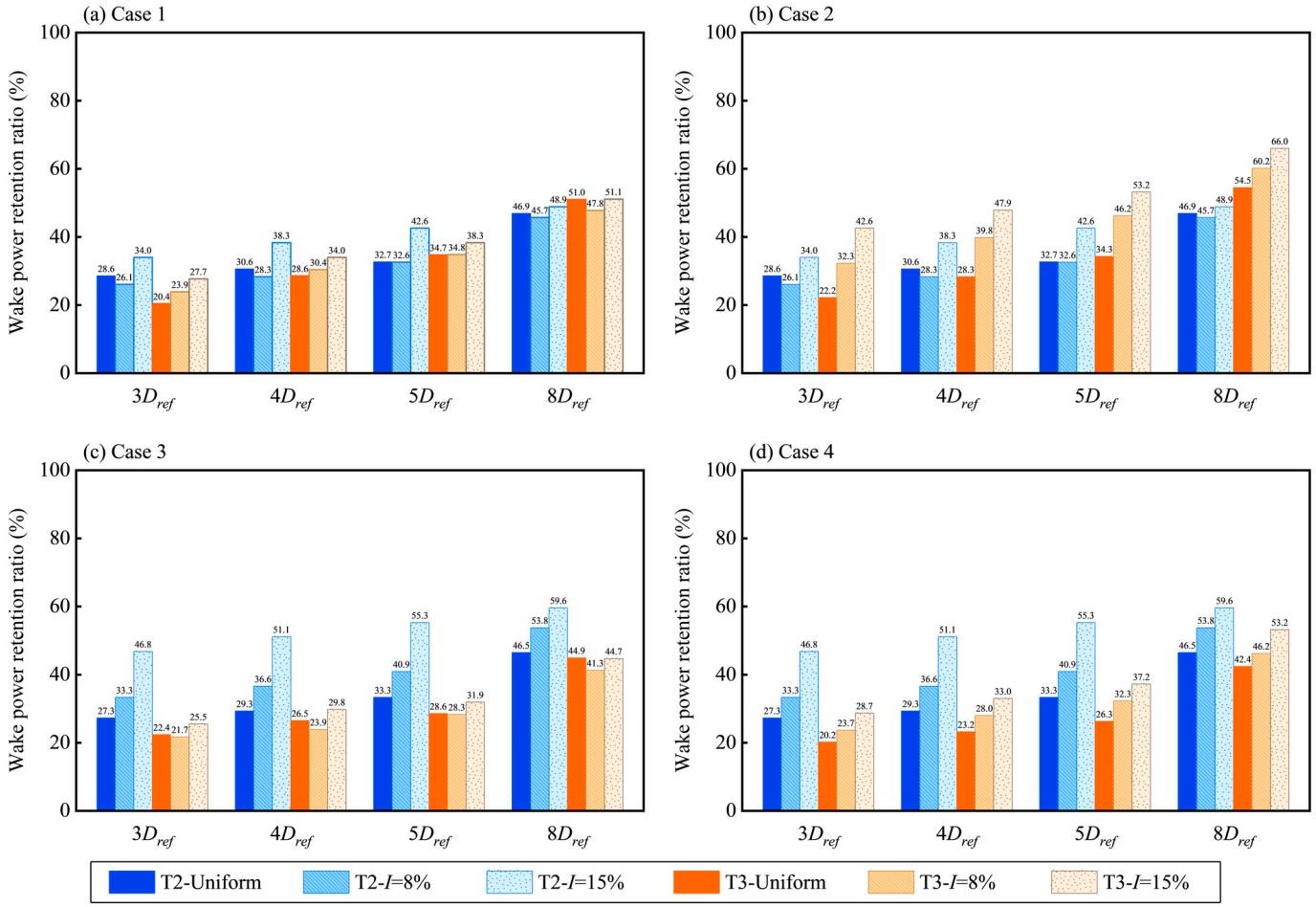


Figure 7. Wake power retention ratios of T2 and T3 under different streamwise spacings and inflow turbulence intensities: (**a**) Case 1; (**b**) Case 2; (**c**) Case 3; and (**d**) Case 4.

Figures 7c and 7d show the corresponding results for Cases 3 and 4. Under uniform inflow, the wake power retention ratios of T2 and T3 in Case 3 increase from 27.3% and 22.4% at $3D_{ref}$ to 46.5% and 44.9% at $8D_{ref}$, respectively. In Case 4, the corresponding values increase from 27.3% and 20.2% to 46.5% and 42.4%. The same increasing trend is observed under both turbulent inflow conditions. For example, under 15% turbulence intensity, the

retention ratios of T2 and T3 increase from 46.8% and 25.5% to 59.6% and 44.7% in Case 3, while those in Case 4 increase from 46.8% and 28.7% to 59.6% and 53.2%, respectively. These findings further confirm that increasing streamwise spacing improves the power retention of downstream turbines regardless of the turbine combination. Moreover, the comparison between Cases 1 and 2 and between Cases 3 and 4 highlights the influence of downstream turbine type on the relative power response. Although the actual power outputs differ because of the different rated capacities and aerodynamic characteristics, the wake power retention ratio provides a more appropriate basis for evaluating their relative responses to wake interference.

The influence of inflow turbulence intensity on wake power retention is also evident in Figure 7. In general, the 15% turbulence cases exhibit higher retention ratios than the corresponding uniform-inflow cases, particularly at relatively small spacing. For instance, at $3D_{ref}$, the retention ratio of T3 in Case 2 increases from 22.2% under uniform inflow to 42.6% under 15% turbulence intensity. Similarly, the retention ratio of T2 in Case 3 increases from 27.3% to 46.8%. This improvement can be associated with enhanced turbulent mixing and momentum exchange across the wake shear layer, which promote the entrainment of higher-momentum fluid into the wake region. However, the effect of 8% turbulence intensity is less consistent. Depending on the turbine configuration and downstream position, the corresponding retention ratios may be higher or lower than those under uniform inflow. This indicates that the influence of ambient turbulence on wake recovery depends on both turbulence intensity and turbine configuration rather than following a simple monotonic relationship. Importantly, because the wake power retention ratio is calculated using the corresponding isolated-turbine reference power under the same inflow condition, the comparison accounts for the direct influence of inflow turbulence on the power generation of each turbine.

To further evaluate the combined effects of streamwise spacing and turbine configuration, the array-level wake power retention ratio is defined as:

$$\eta_{array} = \frac{\sum_{i=1}^{3} P_{i,wake}}{\sum_{i=1}^{3} P_{i,0}} \times 100\% \quad (12)$$

where the numerator represents the total power output of the three turbines operating in the tandem array, and the denominator represents the sum of their corresponding isolated-turbine reference power outputs under identical inflow conditions. This parameter provides an overall assessment of wake-induced power losses while accounting for the different rated capacities of the turbine combinations.

Figure 8 presents the array-level wake power retention ratios under uniform inflow, 8% turbulence intensity, and 15% turbulence intensity. A consistent increase is observed in all four configurations as the spacing increases from $3D_{ref}$ to $8D_{ref}$. Under uniform inflow, the array-level retention ratios increase from 62.4% to 74.6% in Case 1, from 54.7% to 71.3% in Case 2, from 55.5% to 67.6% in Case 3, and from 49.2% to 63.0% in Case 4. Under 8% turbulence intensity, the corresponding values increase from 62.7% to 73.5%, from 58.2% to 73.3%, from 57.8% to 69.8%, and from 52.3% to 66.7%, respectively. Similarly, under 15% turbulence intensity, the retention ratios increase from 65.4% to 75.0% in Case 1, from 63.8% to 76.2% in Case 2, from 63.8% to 72.8% in Case 3, and from 58.5% to 70.9% in Case 4. These results demonstrate that increasing streamwise spacing reduces the overall relative power losses of the tandem array under all investigated inflow conditions.

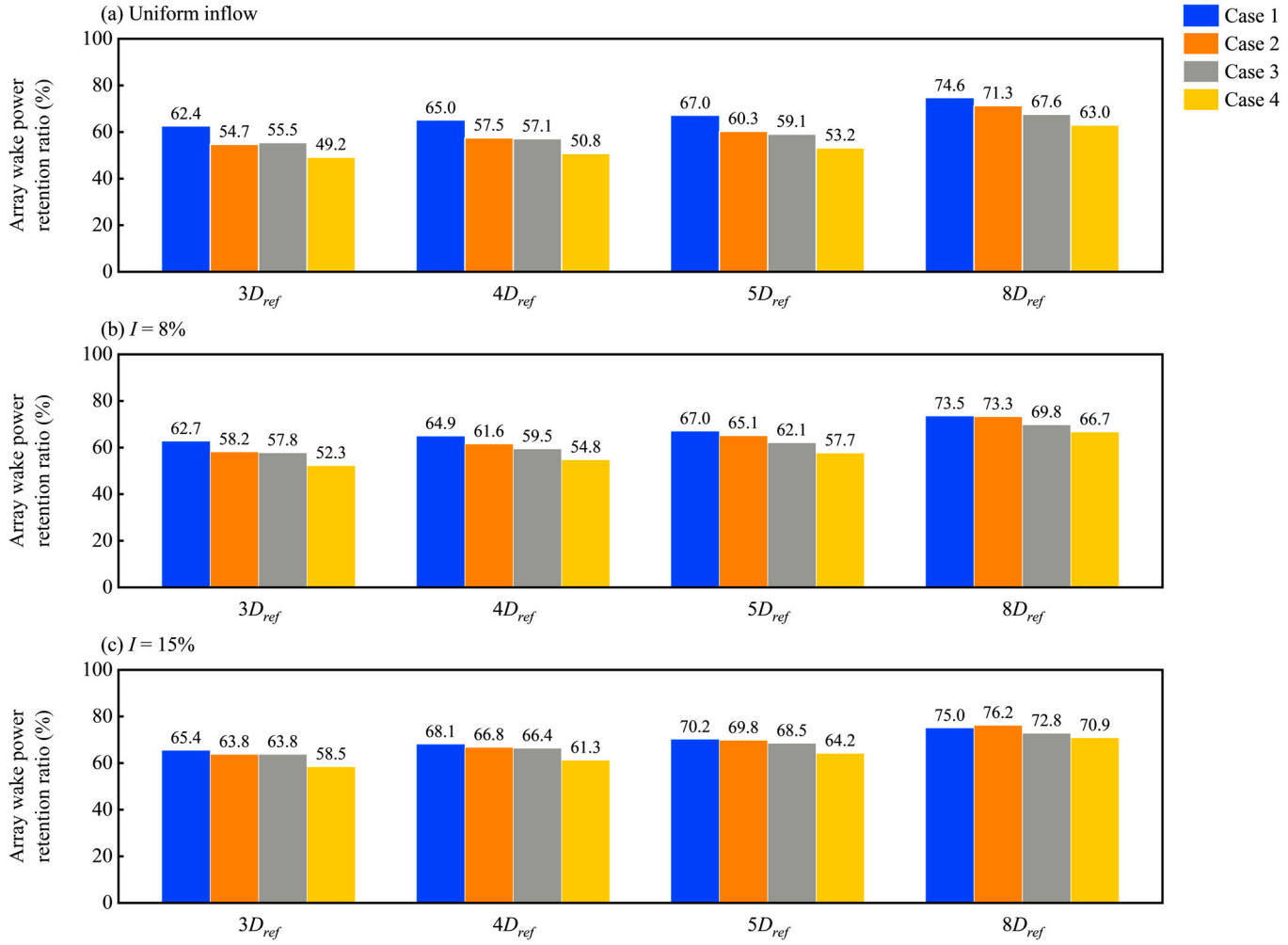


Figure 8. Array-level wake power retention ratios under different streamwise spacings and inflow conditions: (**a**) Uniform inflow; (**b**) I = 8%; and (**c**) I = 15%.

A comparison among the four configurations further reveals that turbine-type arrangement has a considerable influence on the overall wake-related power performance. Under uniform inflow and 8% turbulence intensity, Case 1 generally exhibits a relatively high array-level wake power retention ratio, whereas Case 4 consistently presents the lowest values across the investigated spacings. Under 15% turbulence intensity, Case 2 achieves the highest retention ratio at $8D_{ref}$, reaching 76.2%. This suggests that the combination of turbine types and their associated aerodynamic characteristics affects the cumulative wake interactions within the array. However, a higher absolute array power output does not necessarily correspond to a higherarray-level wake power retention ratio. For example, under uniform inflow at $8D_{ref}$, Case 4 achieves the highest actual array power output of 18.7 MW, whereas its array-level retention ratio is only 63.0%, compared with 74.6% in Case 1. This difference arises because the two configurations have different total rated capacities and isolated-turbine reference power outputs. Therefore, absolute array power and array-level wake power retention ratio should be considered together when evaluating the performance of different turbine combinations.

4.2. Effects of Inflow Conditions on Wake Characteristics

To further investigate the influence of inflow conditions on wake development and downstream aerodynamic performance, Cases 1 and 4 are selected for comparison at a streamwise spacing of $M = 5D_{ref}$. These two configurations represent different turbine-type

combinations at the intermediate and downstream positions, allowing the effects of turbine configuration and inflow turbulence on wake evolution to be examined. The analysis combines the turbine power outputs in Figure 6, the individual wake power retention ratios in Figure 7, the array-level wake power retention ratios in Figure 8, and the wake velocity-deficit contours in Figure 9. The velocity-deficit contours are extracted from a common horizontal XY plane at z = 119 m, corresponding to the hub height of the DTU 10-MW turbine and 29 m above the hub height of the NREL 5-MW turbine. Therefore, this plane provides a consistent horizontal reference for comparing the wake distributions, although it does not pass through the hub center of every turbine type.

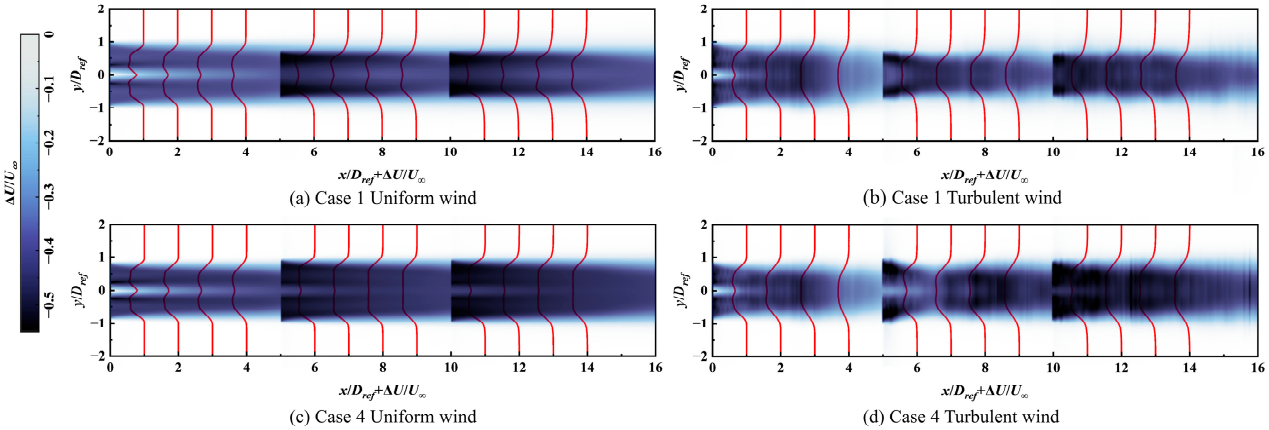


Figure 9. Wake velocity-deficit contours on the horizontal XY plane at z = 119 m for Cases 1 and 4 at $M = 5D_{ref}$ under different inflow conditions: (**a**) Case 1 under uniform inflow; (**b**) Case 1 under 15% turbulence intensity; (**c**) Case 4 under uniform inflow; and (**d**) Case 4 under 15% turbulence intensity.

Under uniform inflow, both configurations exhibit relatively coherent and persistent low-velocity wake regions, as shown in Figure 9a,c. The wake cores maintain pronounced velocity deficits over considerable downstream distances, indicating relatively slow wake recovery. In the absence of ambient turbulence, momentum exchange between the wake and the surrounding flow is primarily driven by turbine-induced turbulence, tip-vortex dissipation, and the natural development of the wake shear layer. Consequently, the entrainment of high-momentum ambient fluid into the wake core is relatively limited, allowing the velocity deficit to persist as the flow travels downstream. This behavior is particularly important in tandem arrays because the downstream turbines are successively exposed to the wakes generated by upstream turbines, resulting in cumulative wake interference.

A comparison between Cases 1 and 4 further reveals the influence of turbine configuration on wake development. In Case 1, T2 is an NREL 5-MW turbine with a rotor diameter of 126 m, whereas T2 in Case 4 is a DTU 10-MW turbine with a rotor diameter of 178.3 m. The smaller rotor of the NREL turbine in Case 1 produces a relatively confined wake region, whereas the larger DTU rotor in Case 4 is associated with a broader velocity-deficit distribution. In Case 1, the wake generated by T2 interacts with the residual wake of T1, but the combined wake exhibits partial spatial recovery before reaching T3. In contrast, the broader wake generated by the DTU 10-MW turbine at T2 in Case 4 overlaps more extensively with the residual wake of T1, forming a more persistent composite low-velocity region between T2 and T3. As a result, T3 is exposed to stronger cumulative wake interference in Case 4 under uniform inflow. It should be noted that these differences reflect the combined effects of rotor diameter, hub height, aerodynamic characteristics, and turbine operating conditions rather than rotor size alone.

The influence of inflow turbulence becomes more pronounced when the turbulence intensity increases to 15%, as illustrated in Figure 9b,d. Compared with uniform inflow, the

wake boundaries become more diffuse, the coherence of the low-velocity cores is weakened, and stronger lateral diffusion and wake meandering are observed. Ambient turbulence enhances turbulent transport across the wake shear layer, promoting the entrainment of high-momentum fluid from the surrounding flow into the low-velocity wake region. This process accelerates the redistribution of momentum, reduces the persistence of the wake velocity deficit, and improves the effective inflow conditions experienced by downstream turbines. Although the overall wake region may become more spatially dispersed, the reduction in the coherent velocity-deficit core indicates enhanced wake mixing and recovery. These characteristics demonstrate that ambient turbulence plays an important role in modifying wake development and reducing the persistence of multiple-wake interference.

The different responses of Cases 1 and 4 to inflow turbulence can also be identified from the wake power retention ratios in Figure 7. At $M = 5D_{ref}$, under uniform inflow, the wake power retention ratios of T2 and T3 in Case 1 are 32.7% and 34.7%, respectively. When the turbulence intensity increases to 8%, the corresponding values are 32.6% and 34.8%, indicating relatively limited changes in the relative power retention of the two downstream turbines. At 15% turbulence intensity, these values increase to 42.6% and 38.3%, respectively. A more pronounced response is observed in Case 4. Under uniform inflow, the retention ratios of T2 and T3 are 33.3% and 26.3%, respectively. These values increase to 40.9% and 32.3% under 8% turbulence intensity and further increase to 55.3% and 37.2% under 15% turbulence intensity. These results indicate that the improvement in downstream power retention induced by ambient turbulence is configuration-dependent. In particular, T2 in Case 4 exhibits a more substantial response to increasing turbulence intensity, suggesting that the wake generated by the intermediate DTU 10-MW turbine is more sensitive to changes in the inflow turbulence conditions under the investigated operating conditions.

The array-level results in Figure 8 further demonstrate the influence of inflow turbulence on the overall wake-related performance. At $M = 5D_{ref}$, the array-level wake power retention ratio of Case 1 increases from 67.0% under uniform inflow to 70.2% under 15% turbulence intensity, while the corresponding value under 8% turbulence intensity remains approximately 67.0%. For Case 4, the array-level retention ratio increases from 53.2% under uniform inflow to 57.7% and 64.2% under 8% and 15% turbulence intensities, respectively. These results indicate that the overall benefit of increased inflow turbulence is more pronounced in Case 4 than in Case 1. This difference is associated with the distinct wake structures generated by the intermediate turbines and their subsequent interactions with the downstream wakes. In particular, the broader and more persistent wake region in Case 4 under uniform inflow provides greater scope for turbulence-enhanced momentum exchange and wake recovery.

It is worth noting that the relationship between inflow turbulence intensity and local wake velocity deficit is not necessarily monotonic at every downstream position. Although higher ambient turbulence generally promotes wake mixing and reduces the persistence of the coherent velocity-deficit core, stronger turbulent fluctuations and enhanced momentum extraction can also produce pronounced local velocity deficits immediately downstream of a rotor. Therefore, a local low-velocity region in the near wake does not necessarily indicate poorer turbine performance. The spatial distribution of velocity deficits should be interpreted together with the downstream power output and wake power retention ratios to obtain a more comprehensive understanding of the aerodynamic response.

4.3. Effects of Turbine-Type Arrangement on Wake Characteristics

To further investigate the influence of turbine-type arrangement on wake development and downstream aerodynamic performance, Cases 2 and 3 are selected for comparison. These two configurations contain the same turbine composition, consisting of two DTU

10-MW turbines and one NREL 5-MW turbine, but differ in the arrangement of the intermediate and downstream turbines. Specifically, Case 2 places the NREL 5-MW turbine at T2 and the DTU 10-MW turbine at T3, whereas Case 3 reverses their positions. Both configurations have an identical total rated capacity of 25 MW. The comparison is conducted at a representative streamwise spacing of $M = 5D_{ref}$. Figures 10 and 11 present the wake velocity-deficit distributions on vertical YZ planes at six streamwise locations under uniform and turbulent inflow with a turbulence intensity of 15%. The same color scale is used in both figures, allowing the spatial distributions and relative magnitudes of the velocity deficits to be compared directly. The analysis is further supported by the turbine-specific wake power retention ratios in Figure 7 and the array-level results in Figure 8.

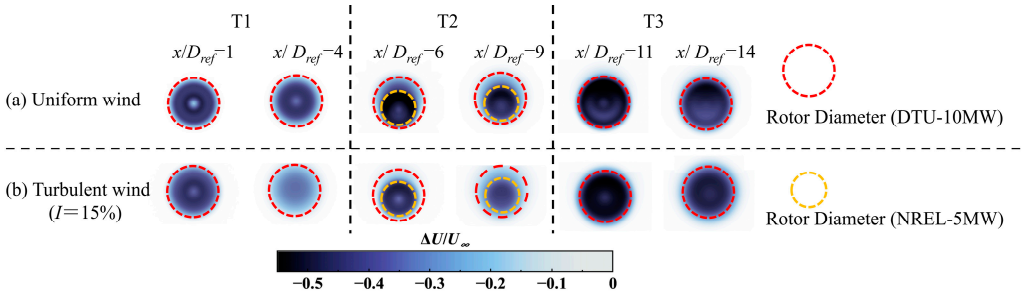


Figure 10. Wake velocity-deficit distributions at different streamwise locations for Case 2 under (**a**) uniform inflow and (**b**) turbulent inflow ($I = 15\%$).

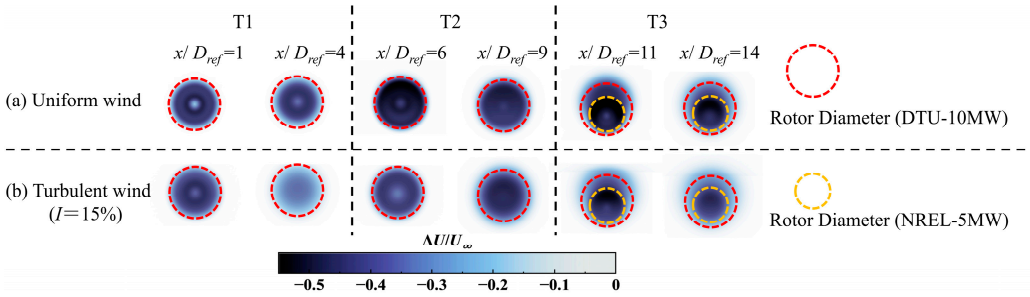


Figure 11. Wake velocity-deficit distributions at different streamwise locations for Case 3 under (**a**) uniform inflow and (**b**) turbulent inflow ($I = 15\%$).

As shown in Figures 10 and 11, the wake distributions behind the upstream turbine T1 are generally consistent between the two configurations. This is expected because T1 is the same DTU 10-MW turbine in both cases, with identical geometric and operating characteristics. At $x/D_{ref} = 1$, a pronounced velocity-deficit core develops immediately downstream of T1. As the wake propagates to $x/D_{ref} = 4$, the low-velocity region gradually expands and becomes less concentrated. Under turbulent inflow with a turbulence intensity of 15%, the wake boundaries become more diffuse, indicating enhanced momentum exchange between the wake shear layer and the surrounding flow. The similarity of the upstream wake distributions provides a consistent reference for examining the subsequent differences caused by the turbine-type arrangement at T2 and T3.

More pronounced differences emerge in the wake region behind the intermediate turbine T2. In Case 2, T2 is the NREL 5-MW turbine, with a rotor diameter of 126 m and a hub height of 90 m. As shown in Figure 10, the velocity-deficit region at $x/D_{ref} = 6$ is relatively concentrated, corresponding to the smaller rotor-swept area of the intermediate turbine. Further downstream, at $x/D_{ref} = 9$, the wake becomes more diffuse and the central velocity deficit is reduced, indicating partial momentum recovery before the flow reaches T3. In contrast, T2 in Case 3 is the DTU 10-MW turbine, with a larger rotor diameter of

178.3 m and a higher hub height of 119 m. Figure 11 shows a broader velocity-deficit distribution behind this turbine, particularly at $x/D_{ref} = 6$. Although the wake gradually develops and recovers as it propagates toward $x/D_{ref} = 9$, a relatively extensive low-velocity region remains. The comparison therefore indicates that replacing the intermediate NREL 5-MW turbine with the DTU 10-MW turbine changes both the spatial extent and vertical distribution of the wake. These differences reflect the combined effects of rotor dimensions, hub height, aerodynamic loading, and turbine operation rather than rotor diameter alone.

The differences in the intermediate wake further influence the effective inflow conditions experienced by T3. The cross-section at $x/D_{ref} = 9$ is particularly important because it represents the flow immediately upstream of the downstream turbine. In Case 2, the relatively confined wake generated by the intermediate NREL 5-MW turbine affects a comparatively limited region of the incoming flow to T3. Moreover, the hub height of T2 is 90 m, whereas that of the downstream DTU 10-MW turbine is 119 m, resulting in a vertical offset of 29 m between the rotor axes. Consequently, the residual wake from T2 does not necessarily affect the entire swept area of T3 uniformly, and portions of the downstream rotor may receive relatively higher-momentum inflow. In Case 3, the intermediate DTU 10-MW turbine generates a wake with a larger spatial extent, while the downstream NREL 5-MW turbine has a lower hub height of 90 m. Although the two turbines also have a 29-m hub-height difference, their rotor-swept areas exhibit substantial vertical overlap. The broader wake generated by T2 therefore affects a considerable portion of the downstream flow field, resulting in more pronounced wake exposure for T3. This comparison demonstrates that the interaction between wake extent and rotor-swept-area overlap is an important factor governing the aerodynamic response of heterogeneous tandem turbine arrays.

The wake distributions downstream of T3 provide additional evidence of the influence of turbine-type arrangement on the spatial evolution of the flow. At $x/D_{ref} = 11$, a pronounced low-velocity region is observed behind T3 in both configurations. This feature primarily represents the near wake generated by the downstream turbine itself as a consequence of momentum extraction, rather than the incoming velocity deficit experienced by T3. At $x/D_{ref} = 14$, the low-velocity regions become more diffuse, indicating further wake expansion and momentum recovery. A notable distinction is observed in the vertical position of the wake core. In Case 2, T3 is a DTU 10-MW turbine with a hub height of 119 m, whereas in Case 3, T3 is an NREL 5-MW turbine with a hub height of 90 m. Accordingly, the wake generated by T3 in Case 3 exhibits a lower vertical position than that in Case 2, consistent with the 29-m difference in their hub heights. This observation confirms that turbine-type arrangement affects not only the magnitude and spatial extent of the wake but also its vertical distribution. Therefore, the vertical position of the wake relative to the downstream rotor should be considered when evaluating wake interactions in heterogeneous turbine arrays.

The influence of inflow turbulence is also evident in both configurations. Compared with uniform inflow, the 15% turbulence condition produces more diffuse wake boundaries and weakens the coherence of the low-velocity cores, particularly at the downstream sections behind T1 and T2. The enhanced ambient turbulence promotes momentum transport across the wake shear layers and facilitates the entrainment of high-momentum fluid into the wake regions. Consequently, the velocity deficits become less spatially concentrated as the flow develops downstream. Nevertheless, pronounced low-velocity regions remain immediately behind T3 at $x/D_{ref} = 11$ because of the momentum extracted by the downstream turbine. Their subsequent diffusion at $x/D_{ref} = 14$ demonstrates the continuing development and recovery of the newly generated wake. These observations indicate that ambient turbulence modifies wake evolution in both arrangements, while the spatial distribution of the velocity deficit remains dependent on the turbine type and its position within the array.

The power results in Figure 7 further quantify the aerodynamic differences between the two arrangements. Under uniform inflow at $M = 5D_{ref}$, the wake power retention ratios of T2 and T3 in Case 2 are 32.7% and 34.3%, respectively. In Case 3, the corresponding values are 33.3% and 28.6%. When the turbulence intensity increases to 8%, the retention ratios in Case 2 become 32.6% for T2 and 46.2% for T3, whereas those in Case 3 reach 40.9% and 28.3%, respectively. Under 15% turbulence intensity, Case 2 exhibits retention ratios of 42.6% and 53.2% for T2 and T3, respectively. The corresponding values in Case 3 are 55.3% and 31.9%. These results reveal a clear redistribution of power generation between the intermediate and downstream turbines. In particular, placing the DTU 10-MW turbine at T3 in Case 2 results in a substantially higher downstream power retention ratio than placing the NREL 5-MW turbine at T3 in Case 3 under the investigated conditions. This difference is consistent with the distinct wake distributions and rotor-height relationships observed in Figures 10 and 11. It should be noted that the retention ratios are calculated relative to the corresponding isolated-turbine reference powers under matched inflow conditions and therefore represent turbine-specific relative power performance rather than absolute power differences.

The array-level results in Figure 8 provide a more comprehensive assessment of the two turbine-type arrangements. At $M = 5D_{ref}$, the total power outputs of Cases 2 and 3 are 14.9 and 14.6 MW under uniform inflow, respectively. Under 8% turbulence intensity, the corresponding outputs are 15.1 and 14.4 MW, while under 15% turbulence intensity they increase to 16.4 and 16.1 MW, respectively. Although the downstream turbine in Case 2 exhibits a substantially higher power output than that in Case 3, the differences in total array power remain relatively small. For example, under 15% turbulence intensity, T3 produces 5.0 MW in Case 2 and 1.5 MW in Case 3, corresponding to a difference of 3.5 MW. However, the total array power differs by only 0.3 MW. This is because the intermediate DTU 10-MW turbine in Case 3 produces 5.2 MW, compared with 2.0 MW from the intermediate NREL 5-MW turbine in Case 2. Thus, the increased power generation at T2 in Case 3 largely compensates for the reduction in T3 output. These results demonstrate that turbine-type arrangement can substantially affect the distribution of power generation among individual turbines without necessarily producing an equally pronounced change in the total array output.

Positioning the NREL 5-MW turbine at T2 and the DTU 10-MW turbine at T3 results in a relatively confined intermediate wake and higher relative power retention at the downstream turbine under the investigated conditions. Conversely, placing the DTU 10-MW turbine at T2 produces a broader wake that affects a larger portion of the downstream flow field, resulting in a lower relative power retention at T3. However, the resulting changes in individual turbine outputs are partially compensated within the array, and the differences in total power between the two arrangements remain comparatively small. Therefore, the selection of turbine-type arrangements for heterogeneous tandem wind turbine arrays should consider both the local wake characteristics and the overall power distribution across the entire array rather than evaluating downstream turbine performance in isolation.

4.4. Overall Power Performance of the Tandem Array

To evaluate the overall power performance of the tandem array, the total time-averaged power output is calculated as the sum of the mean power outputs of the three turbines:

$$P_{total} = P_1 + P_2 + P_3 \tag{13}$$

To account for differences in installed rated capacity among the seven configurations, the rated-capacity-normalized array power output is defined as:

$$R_{total} = \frac{P_{total}}{P_{r,1} + P_{r,2} + P_{r,3}} \times 100\% \quad (14)$$

where P_1, P_2, and P_3 denote the time-averaged power outputs of T1, T2, and T3 over the final 1000 s, respectively; $P_{r,i}$ represents the rated power of turbine i; and R_{total} is the ratio of the total time-averaged array power output to the total installed rated capacity, expressed as a percentage. Unlike the array-level wake power retention ratio defined in Section 4.1, which is normalized by the sum of the corresponding isolated-turbine reference powers under identical inflow conditions, R_{total} characterizes the utilization of installed rated capacity rather than wake-induced power losses. Table 4 summarizes the total time-averaged power output and rated-capacity-normalized output for all simulated configurations.

Table 4. Total time-averaged power output and rated-capacity-normalized array power output of the tandem array under all simulated configurations.

Case	Rated Capacity (MW)	M/D_{ref}	Ptotal (MW) I = 0%	Rtotal (%) I = 0%	Ptotal (MW) I = 8%	Rtotal (%) I = 8%	Ptotal (MW) I = 15%	Rtotal (%) I = 15%
Case 1	20	3	12.3	61.5	11.6	58.0	12.3	61.5
Case 1	20	4	12.8	64.0	12.0	60.0	12.8	64.0
Case 1	20	5	13.2	66.0	12.4	62.0	13.2	66.0
Case 1	20	8	14.7	73.5	13.6	68.0	14.1	70.5
Case 2	25	3	13.5	54.0	13.5	54.0	15.0	60.0
Case 2	25	4	14.2	56.8	14.3	57.2	15.7	62.8
Case 2	25	5	14.9	59.6	15.1	60.4	16.4	65.6
Case 2	25	8	17.6	70.4	17.0	68.0	17.9	71.6
Case 3	25	3	13.7	54.8	13.4	53.6	15.0	60.0
Case 3	25	4	14.1	56.4	13.8	55.2	15.6	62.4
Case 3	25	5	14.6	58.4	14.4	57.6	16.1	64.4
Case 3	25	8	16.7	66.8	16.2	64.8	17.1	68.4
Case 4	30	3	14.6	48.7	14.6	48.7	16.5	55.0
Case 4	30	4	15.1	50.3	15.3	51.0	17.3	57.7
Case 4	30	5	15.8	52.7	16.1	53.7	18.1	60.3
Case 4	30	8	18.7	62.3	18.6	62.0	20.0	66.7
Case 5	20	3	10.1	50.5				
Case 5	20	4	10.5	52.5				
Case 5	20	5	10.9	54.5				
Case 6	20	3	10.7	53.3				
Case 6	20	4	11.2	56.0		-		
Case 6	20	5	11.6	58.0				
Case 7	25	3	11.6	46.4				
Case 7	25	4	12.2	48.8				
Case 7	25	5	12.8	51.2				

Note: I = 0% denotes uniform inflow. Cases 1–4 include I = 0%, 8%, and 15% at M = 3, 4, 5, and 8D_{ref}. Cases 5–7 include uniform inflow only at M = 3, 4, and 5D_{ref}. Total powers are rounded to 0.1 MW; normalized percentages are retained from the underlying mean values.

Under identical total rated capacities and inter-turbine spacing ratios, the configurations with a DTU 10-MW turbine in the first row consistently achieved higher total average power outputs. For arrays with a total rated capacity of 20 MW, the power outputs of Case 1 were 21.1–21.9% and 13.8–15.0% higher than those of Cases 5 and 6, respectively. For arrays

with a total rated capacity of 25 MW, the power outputs of Cases 2 and 3 were 16.4% and 14.1–18.1% higher than that of Case 7, respectively. These results demonstrate that placing a DTU 10-MW turbine in the first row provides better overall power generation performance across different total rated capacities and inter-turbine spacing conditions. Therefore, the DTU 10-MW turbine was selected as the first-row turbine in this study.

For Cases 1–4, the total array power increases consistently with streamwise spacing under all three inflow conditions. Under uniform inflow, the total power of Case 1 increases from 12.3 MW at $3D_{ref}$ to 14.7 MW at $8D_{ref}$, while that of Case 4 increases from 14.6 to 18.7 MW. Similar trends are observed in Cases 2 and 3. The continued increase in total power from $5D_{ref}$ to $8D_{ref}$ indicates that array-level power recovery has not reached saturation within the investigated spacing range.

The effect of inflow turbulence on total array power is configuration-dependent. Under 15% turbulence intensity, Cases 2–4 consistently produce higher total power than under uniform inflow at all four spacings. In contrast, Case 1 exhibits nearly identical outputs under the two conditions at $3D_{ref}$–$5D_{ref}$, but a decrease from 14.7 to 14.1 MW at $8D_{ref}$. The response to 8% turbulence intensity is also non-uniform, depending on turbine configuration and spacing. These results indicate that the array-level response is governed by the combined power outputs of all three turbines, and that improvements in downstream power generation do not necessarily compensate for changes in upstream turbine output.

Comparisons among configurations with identical turbine compositions and rated capacities further demonstrate the influence of turbine-type arrangement. In the 20-MW group (Cases 1, 5, and 6), Case 1 consistently achieves the highest total power under uniform inflow at all three common spacings, followed by Case 6 and Case 5. In the 25-MW group (Cases 2, 3, and 7), Case 3 produces the highest output at $3D_{ref}$ (13.7 MW), whereas Case 2 leads at $4D_{ref}$ and $5D_{ref}$, with outputs of 14.2 and 14.9 MW, respectively. Case 7 exhibits the lowest output throughout. These comparisons demonstrate that the effect of turbine-type arrangement is coupled with streamwise spacing, and that the relative performance of different arrangements can vary with spacing.

The comparison between Cases 2 and 3 further illustrates the redistribution of power within the array. At $5D_{ref}$ under 15% turbulence intensity, their total power outputs are 16.4 and 16.1 MW, respectively, differing by only 0.3 MW. However, the individual outputs of T2 and T3 differ substantially: T2 produces 2.0 MW in Case 2 and 5.2 MW in Case 3, whereas T3 produces 5.0 and 1.5 MW, respectively. The higher output of T2 in Case 3 largely compensates for its lower T3 output, resulting in a relatively small difference in total array power. This finding highlights the importance of evaluating turbine-type arrangement at both individual and array levels.

Case 4 produces the highest absolute total power among Cases 1–4 under corresponding spacing and inflow conditions. For example, at $8D_{ref}$ under uniform inflow, its output reaches 18.7 MW, compared with 14.7, 17.6, and 16.7 MW for Cases 1, 2, and 3, respectively. However, Case 4 also has the largest installed rated capacity (30 MW). After rated-capacity normalization, it exhibits the lowest output among these four configurations under the corresponding conditions. At $8D_{ref}$ under uniform inflow, its rated-capacity-normalized power output is 62.3%, compared with 73.5%, 70.4%, and 66.8% for Cases 1, 2, and 3, respectively. Therefore, the highest absolute power output does not necessarily indicate the highest utilization of installed capacity. Both absolute power generation and rated-capacity-normalized array power output should be considered when evaluating heterogeneous turbine arrays.

4.5. Scope and Limitations

This study investigates the wake characteristics and power performance of heterogeneous three-turbine tandem arrays composed of NREL 5-MW and DTU 10-MW wind

turbines. A total of 57 configurations are examined to evaluate the effects of streamwise spacing, inflow turbulence intensity, and turbine-type arrangement on individual turbine power output and overall array performance. The results provide insights into wake interactions and power redistribution in heterogeneous tandem arrays.

Several limitations should be acknowledged. First, the investigation is restricted to two turbine models and three-turbine tandem configurations, with inflow conditions limited to uniform inflow and turbulence intensities of 8% and 15%. Atmospheric stability, vertical wind shear, wind direction variations, and yaw misalignment are not considered. Second, detailed wake-field comparisons are conducted only for selected configurations and inflow conditions, rather than all 57 simulated cases. In addition, the performance evaluation is primarily based on time-averaged power over the final 1000 s, without explicitly quantifying statistical uncertainty from independent turbulent realizations or assessing structural loads. The investigated spacing range also does not establish the distance at which wake recovery reaches saturation. The quantitative discrepancies discussed in Section 2.3.3 should also be considered when interpreting absolute wake-induced power losses and small differences in power output between turbine configurations.

Future work will extend the investigation to more diverse turbine combinations and larger array configurations, incorporating broader atmospheric conditions and wind directions. Further studies will also consider larger streamwise spacings, three-dimensional time-resolved wake analyses, multiple turbulent realizations, and structural load assessments to improve the understanding of wake interactions and the long-term performance of heterogeneous offshore wind turbine arrays.

5. Conclusions

This study examines an offshore three-turbine tandem array composed of DTU 10-MW and NREL 5-MW wind turbines. Numerical simulations are performed for different streamwise spacings, inflow conditions, and turbine-type combinations and arrangements to characterize turbine power output and wake evolution. The main conclusions are as follows:

(1) Increasing streamwise spacing effectively reduces wake interference and improves downstream turbine power output. As the spacing increases from $3D_{ref}$ to $8D_{ref}$, the power outputs and wake power retention ratios of T2 and T3 increase consistently across all four configurations, while T1 remains nearly unchanged. The array-level wake power retention ratio also increases under all investigated inflow conditions, indicating that wake recovery has not reached saturation within the tested spacing range.

(2) Inflow turbulence promotes wake diffusion and momentum exchange, thereby generally improving downstream power recovery, particularly at 15% turbulence intensity. However, the effect of 8% turbulence intensity is configuration-dependent. Moreover, improved downstream power generation does not necessarily increase total array power, as changes in upstream turbine output may offset the downstream gains.

(3) Turbine-type arrangement significantly affects wake development and power redistribution. Comparisons between Cases 2 and 3 demonstrate that changing the positions of the NREL 5-MW and DTU 10-MW turbines modifies wake expansion, vertical distribution, and downstream rotor exposure. At $5D_{ref}$ under 15% turbulence intensity, the wake power retention ratios of T3 are 53.2% and 31.9% in Cases 2 and 3, respectively. Nevertheless, their total array power outputs differ by only 0.3 MW, demonstrating that substantial differences in individual turbine performance can be partially compensated within the array.

(4) The overall power performance is governed by the combined effects of turbine composition, arrangement, and streamwise spacing. Comparisons among configurations with identical turbine compositions and rated capacities show that turbine positioning sub-

stantially influences total power generation. Furthermore, the highest absolute array power does not necessarily correspond to the highest rated-capacity-normalized array power output. Therefore, both total power generation and normalized performance indicators should be considered when evaluating heterogeneous wind turbine arrays.

Overall, these findings highlight the importance of jointly optimizing turbine-type arrangement and streamwise spacing to mitigate cumulative wake interference and improve the power performance of heterogeneous offshore wind turbine arrays.

Author Contributions: Conceptualization, J.T.; methodology, Z.Z. and J.T.; software, C.H.; validation, C.H., H.H., J.T., Z.Z. and Z.H.; formal analysis, J.T. and Z.Z.; investigation, Z.Z., J.J. and Z.S.; resources, Z.H.; data curation, C.H. and H.H.; writing—original draft, C.H.; writing—review & editing, C.H., H.H., J.J., J.T. and Z.H.; visualization, C.H. and J.T.; supervision, Z.Z. and J.T.; project administration, Z.S., J.T. and Z.H.; funding acquisition, J.T. and Z.H. All authors have read and agreed to the published version of the manuscript.

Funding: This research was funded by the National Natural Science Foundation of China (No. 52371285), the Hunan Provincial Natural Science Foundation (No. 2025JJ50306), and the National College Student Innovation and Entrepreneurship Training Program Project (202610530054).

Data Availability Statement: The original contributions presented in this study are included in the article material. Further inquiries can be directed to the corresponding author.

Conflicts of Interest: The authors declare no conflicts of interest.

Appendix A. Reproducibility Parameters

Tables A1–A3 summarize the key TurbSim and FAST.Farm settings used in the numerical experiments, including the inflow-generation, computational-domain, turbine-layout, DWM, and wake-superposition parameters. Output-only options and inactive model settings are omitted for clarity.

Table A1. Key TurbSim inflow-generation parameters.

Parameter	Value Used	Definition or Implementation Note
TurbSim version	v2.00. *	Full-field stochastic inflow generator.
RandSeed1; *RandSeed2*	123456; 789012	Fixed seeds for reproducible turbulence realization.
$Turb_{Model}$	IECKAI	IEC Kaimal spectra for the u, v, and w components.
IECstandard; *IECWindType*	3; NTM	IEC 61400-3 normal-turbulence condition.
IEC_{turbc}	8% or 15%	Target inflow turbulence-intensity cases considered in the study.
ScaleIEC	0	No post-generation rescaling to an exact standard deviation.
WindProfileType	default ≥ IEC	Power-law profile over the rotor disk and logarithmic profile outside it.
PLExp; Z_0	0.14; 0.03 m	Resolved IEC offshore power-law exponent and surface roughness.
RefHt; *URef*	119 m; 11.4 m s^{-1}	Reference height and mean streamwise velocity.
$NumGrid_Z$; $NumGrid_Y$	47; 400	Vertical and lateral grid-point counts.
GridHeight; *GridWidth*	235 m; 2000 m	Vertical and lateral full-field dimensions.
TimeStep	0.1 s	TurbSim output time increment.
AnalysisTime; *UsableTime*	2100 s; ALL	Analyzed record length and usable output duration.

Note: * denotes the TurbSim v2.00 executable used to generate all turbulent inflow fields in this study.

Table A2. Key FAST.Farm domain and turbine-layout parameters.

Parameter	Value Used	Definition or Implementation Note
$TMax$	2000 s	FAST.Farm simulation duration.
$Mod_{AmbWind}$	2	One InflowWind instance supplies the ambient full-field wind.
DT_{Low}; DT_{High}	1.0 s; 0.1 s	Low- and high-resolution interpolation time steps.
NX_{Low}; NY_{Low}; NZ_{Low}	801; 401; 47	Low-resolution wind-domain node counts.
$X0_{Low}$; $Y0_{Low}$; $Z0_{Low}$	0; −1000; 1.5 m	Low-resolution domain origin.
dX_{Low}; dY_{Low}; dZ_{Low}	5; 5; 5 m	Low-resolution spatial increments.
NX_{High}; NY_{High}; NZ_{High}	41; 41; 46	High-resolution node counts around each turbine.
dX_{High}; dY_{High}; dZ_{High}	5; 5; 5 m	High-resolution spatial increments.

Table A3. Key FAST.Farm DWM and wake-superposition parameters.

Parameter	Value Used	Definition or Implementation Note
Mod_{Wake}	1	Polar dynamic-wake-meandering formulation.
d_r; Num_{Radii}; Num_{Planes}	5 m; 56; 2000	Radial increment, radial-node count, and maximum downstream wake-plane count.
f_c	0.17 Hz	Low-pass cutoff for wake advection, deflection, and meandering.
$C_{NearWake}$; $Mod_{WakeDiam}$; WAT	1.8; 1; 0	Near-wake correction; rotor-diameter wake width; wake-added-turbulence box disabled.
k_{vAmb}	[0.05, 1.0, 0.0, 1.0, 0.01]	Ambient-turbulence eddy-viscosity coefficients.
k_{vShr}	[0.016, 0.2, 3.0, 25.0, 0.1]	Shear-layer eddy-viscosity coefficients.
$Mod_{Meander}$; $C_{Meander}$	3; 1.9	Windowed-jinc meandering filter and calibration coefficient.

Appendix B. Nomenclature

Table A4. Symbols and units used in the manuscript.

Symbol	Meaning	Unit or Convention
D_r	Actual rotor diameter of a specified turbine	m; NREL 126, DTU 178.3
D_{ref}	Common reference rotor diameter	126 m
M	Streamwise center-to-center spacing between adjacent turbines	m; 378, 504, 630, 1008
x, r	Axial and radial coordinates, respectively	m
I	Streamwise inflow turbulence intensity $\sigma_{\square}/U_{mean}$	Dimensionless; reported as % at a reference height of 119 m
U_∞, U_d, U_w	Upstream, rotor-plane and far-wake velocities in momentum theory	m s^{-1}
V_x, V_r	Axial and radial mean velocities in wake equations	m s^{-1}
V_t	Kinematic eddy viscosity	m^2 s^{-1}
α; a_{avg}	Axial induction factor; rotor-disk-averaged axial induction factor	Dimensionless; Dimensionless
ρ; A_d	Air density; rotor-disk area	kg m^{-3}; m^2
τ_1; f_c	Characteristic time scale; cutoff frequency as defined in Equations (7) and (8)	s; Hz
P_i; $P_{r,i}$; P_{total}	Time-averaged power output of turbine i; Rated power of turbine i; Total time-averaged power output of the three-turbine array	MW
C_p; C_T	Power and thrust coefficients	Dimensionless
R_{total}	Ratio of total time-averaged array power output to total installed rated capacity	Dimensionless; reported in percent

References

1. International Energy Agency (IEA). *Renewables 2024: Analysis and Forecasts to 2030*; International Energy Agency: Paris, France, 2024.
2. Global Wind Energy Council (GWEC). *Global Wind Report 2025*; Global Wind Energy Council: Lisbon, Portugal, 2025.
3. Porté-Agel, F.; Bastankhah, M.; Shamsoddin, S. Wind-Turbine and Wind-Farm Flows: A Review. *Bound.-Layer Meteorol.* **2020**, *174*, 1–59. [CrossRef] [PubMed]
4. Stevens, R.J.A.M.; Gayme, D.F.; Meneveau, C. Effects of Turbine Spacing on the Power Output of Extended Wind-Farms. *Wind Energy* **2016**, *19*, 359–370. [CrossRef]
5. Niayifar, A.; Porté-Agel, F. Analytical Modeling of Wind Farms: A New Approach for Power Prediction. *Energies* **2016**, *9*, 741. [CrossRef]
6. Bastankhah, M.; Porté-Agel, F. A New Analytical Model for Wind-Turbine Wakes. *Renew. Energy* **2014**, *70*, 116–123. [CrossRef]
7. Baas, P.; Verzijlbergh, R.A.; van Dorp, P.; Jonker, H.J.J. Investigating Energy Production and Wake Losses of Multi-Gigawatt Offshore Wind Farms with Atmospheric Large-Eddy Simulation. *Wind Energy Sci.* **2023**, *8*, 787–805. [CrossRef]
8. Bay, C.J.; Fleming, P.; Doekemeijer, B.; King, J.; Churchfield, M.; Mudafort, R. Addressing Deep Array Effects and Impacts to Wake Steering with the Cumulative-Curl Wake Model. *Wind Energy Sci.* **2023**, *8*, 401–419. [CrossRef]
9. Kirby, A.; Nishino, T.; Lanzilao, L.; Dunstan, T.D.; Meyers, J. Turbine- and Farm-Scale Power Losses in Wind Farms: An Alternative to Wake and Farm Blockage Losses. *Wind Energy Sci.* **2025**, *10*, 435–450. [CrossRef]
10. Wang, G.; Huang, J.; Zhang, Z.; Chen, K.; Shen, Z.; Tu, J.; Han, Z. Influence of Layout on Offshore Wind Farm Efficiency and Wake Characteristics in Turbulent Environments. *J. Mar. Sci. Eng.* **2025**, *13*, 2137. [CrossRef]
11. Vahidi, D.; Porté-Agel, F. A Physics-Based Model for Wind Turbine Wake Expansion in the Atmospheric Boundary Layer. *J. Fluid Mech.* **2022**, *943*, A49. [CrossRef]
12. Hodgson, E.L.; Madsen, M.H.A.; Andersen, S.J. Effects of Turbulent Inflow Time Scales on Wind Turbine Wake Behavior and Recovery. *Phys. Fluids* **2023**, *35*, 095125. [CrossRef]
13. Gambuzza, S.; Ganapathisubramani, B. The Influence of Free Stream Turbulence on the Development of a Wind Turbine Wake. *J. Fluid Mech.* **2023**, *963*, A19. [CrossRef]
14. Hu, H.; Shen, Z.; Zhang, Z.; Jia, J.; Han, Z.; Tu, J. Numerical Investigation of the Aerodynamic Performance and Wake Evolution of a Coaxial Co-Rotating Dual-Rotor Wind Turbine. *Energy Convers. Manag.* **2026**, *369*, 122055. [CrossRef]
15. Sun, H.; Yang, H. Wind Farm Layout and Hub Height Optimization with a Novel Wake Model. *Appl. Energy* **2023**, *348*, 121554. [CrossRef]
16. Sun, H.; Yang, H.; Tao, S. Optimization of the Number, Hub Height and Layout of Offshore Wind Turbines. *J. Mar. Sci. Eng.* **2023**, *11*, 1566. [CrossRef]
17. Ciavarra, A.W.; Rodrigues, R.V.; Dykes, K.; Réthoré, P.E. Wind Farm Optimization with Multiple Hub Heights Using Gradient-Based Methods. *J. Phys. Conf. Ser.* **2022**, *2265*, 022012. [CrossRef]
18. Feng, J.; Shen, W.Z. Design Optimization of Offshore Wind Farms with Multiple Types of Wind Turbines. *Appl. Energy.* **2017**, *205*, 1283–1297. [CrossRef]
19. Stanley, A.P.J.; Ning, A. Coupled Wind Turbine Design and Layout Optimization with Nonhomogeneous Wind Turbines. *Wind Energy Sci.* **2019**, *4*, 99–114. [CrossRef]
20. Zhang, L.D.; Feng, Z.C.; Song, C.P.; Tian, W.X.; Hu, T.Y.; Guo, Y.J.; Yang, Z.L.; Zhao, X.Y.; Feng, J.Z.; Ren, H.H.; et al. Wind Tunnel Experimental Investigation of Wake Characteristics and Turbulent Mixing in Tandem-Arranged Wind Turbines. *Ocean Eng.* **2025**, *317*, 119967. [CrossRef]
21. Huang, C.N.; Lin, Z.C.; Li, Y.K.; Xie, J.H.; Wang, L.; Yang, J.; Song, D.R.; Chen, S.F. Hybrid Offshore Wind Farm Wake Optimization with Multi-Type Wind Turbines. *J. Mar. Sci. Eng.* **2026**, *14*, 674. [CrossRef]
22. He, G.; Sun, H.; He, R. A Novel Analytical Wake Model for Floating Offshore Wind Turbines with Pitch Motion Effects. *Renew. Energy* **2026**, *256*, 124090. [CrossRef]
23. Malecha, Z.; Dsouza, G. Modeling of Wind Turbine Interactions and Wind Farm Losses Using the Velocity-Dependent Actuator Disc Model. *Computation* **2023**, *11*, 213. [CrossRef]
24. Jonkman, J.; Shaler, K. *FAST.Farm User's Guide and Theory*; Technical Report NREL/TP-5000-78485; National Renewable Energy Laboratory: Golden, CO, USA, 2021.
25. Hao, Y. Wind Farm Wake Modeling and Analysis of Wake Impacts in a Wind Farm. Ph.D. Thesis, University of Massachusetts Amherst, Amherst, MA, USA, 2016. [CrossRef]
26. Shaler, K.; Jonkman, J.; Doubrawa Moreira, P.; Hamilton, N. FAST.Farm Response to Varying Wind Inflow Techniques. In Proceedings of the AIAA SciTech Forum, San Diego, CA, USA, 7–11 January 2019. [CrossRef]
27. Zhang, T.; Xu, X.; Wang, S.; Xing, Y.; Dou, P.; Ji, R.; Zhang, P.; Yang, P. Investigating the Influence of Yaw Control on Wind Farm Dynamic Characteristics for Three Conceptual Floating Offshore Wind Turbines. *Ocean Eng.* **2025**, *339*, 122218. [CrossRef]

28. Xue, L.; Wang, J.; Zhao, L.; Wei, Z.; Yu, M.; Xue, Y. Wake Interactions of Two Tandem Semisubmersible Floating Offshore Wind Turbines Based on FAST. *Farm. J. Mar. Sci. Eng.* **2022**, *10*, 1962. [CrossRef]
29. Jonkman, J.; Butterfield, S.; Musial, W.; Scott, G. *Definition of a 5-MW Reference Wind Turbine for Offshore System Development*; Technical Report NREL/TP-500-38060; National Renewable Energy Laboratory: Golden, CO, USA, 2009. [CrossRef] [PubMed]
30. Bak, C.; Zahle, F.; Bitsche, R.; Kim, T.; Yde, A.; Henriksen, L.C.; Natarajan, A.; Hansen, M.H. *Description of the DTU 10 MW Reference Wind Turbine*; DTU Wind Energy Report-I-0092; Technical University of Denmark, DTU Wind Energy: Roskilde, Denmark, 2013.
31. Barthelmie, R.J.; Hansen, K.; Frandsen, S.T.; Rathmann, O.; Schepers, J.G.; Schlez, W.; Phillips, J.; Rados, K.; Zervos, A.; Politis, E.S.; et al. Modelling and Measuring Flow and Wind Turbine Wakes in Large Wind Farms Offshore. *Wind Energy* **2009**, *12*, 431–444. [CrossRef]
32. Lin, M.; Porté-Agel, F. Large-Eddy Simulation of a Wind-Turbine Array Subjected to Active Yaw Control. *Wind Energy Sci.* **2022**, *7*, 2215–2230. [CrossRef]
33. Türk, M.; Emeis, S. The Dependence of Offshore Turbulence Intensity on Wind Speed. *J. Wind Eng. Ind. Aerodyn.* **2010**, *98*, 466–471. [CrossRef]
34. Emeis, S. Current Issues in Wind Energy Meteorology. *Meteorol. Appl.* **2014**, *21*, 803–819. [CrossRef]
35. Sørum, S.H.; Katsikogiannis, G.; Bachynski-Polić, E.E.; Amdahl, J.; Page, A.M.; Klinkvort, R.T. Fatigue Design Sensitivities of Large Monopile Offshore Wind Turbines. *Wind Energy* **2022**, *25*, 1684–1709. [CrossRef]
36. *IEC 61400-1:2019*; Wind Energy Generation Systems—Part 1: Design Requirements. International Electrotechnical Commission: Geneva, Switzerland, 2019.
37. Kretschmer, M.; Jonkman, J.; Pettas, V.; Cheng, P.W. FAST.Farm Load Validation for Single Wake Situations at Alpha Ventus. *Wind Energy Sci.* **2021**, *6*, 1247–1262. [CrossRef]

Disclaimer/Publisher's Note: The statements, opinions and data contained in all publications are solely those of the individual author(s) and contributor(s) and not of MDPI and/or the editor(s). MDPI and/or the editor(s) disclaim responsibility for any injury to people or property resulting from any ideas, methods, instructions or products referred to in the content.